Applied Catalysis B: Environment and Energy 351 (2024) 123995

Contents lists available at ScienceDirect

Applied Catalysis B: Environment and Energy

journal homepage: www.elsevier.com/locate/apcatb

Manipulating electronic structure of nickel phosphide via asymmetric coordination interaction for anion-exchange membrane based seawater electrolysis

Yanan Xia [a], Lili Guo [a,d], Jiawei Zhu [a,b], Junheng Tang [a,b], Zhipeng Li [a,b], Xiaobin Liu [a,c], Jingqi Chi [a,**], Lei Wang [a,b,*]

[a] Key Laboratory of Eco-chemical Engineering, Ministry of Education, International Science and Technology Cooperation Base of Eco-chemical Engineering and Green Manufacturing, College of Chemical Engineering, Qingdao University of Science and Technology, Qingdao 266042, PR China

[b] College of Chemistry and Molecular Engineering, Qingdao University of Science and Technology, Qingdao 266042, PR China

[c] College of Environment and Safety Engineering, Qingdao University of Science and Technology, Qingdao 266042, PR China

[d] State Key Laboratory of Heavy Oil Processing, College of Chemical Engineering, China University of Petroleum (East China), Qingdao 266580, PR China

ARTICLE INFO

Keywords:
Asymmetric construction
Bifunctional electrocatalyst
Seawater splitting
Anion-exchange membrane water electrolyzer

ABSTRACT

Alkaline seawater electrolysis faces serious problems such as low catalytic activity of bifunctional catalysts and vulnerability to Cl^- corrosion. Hence, Ru-doped nickel phosphide asymmetric structure (Ru-Ni_2P/Ni_5P_4) has been synthesized as highly efficient and corrosion resistant electrocatalysts for alkaline seawater electrolysis at high current density. In-situ characterization technique and DFT calculations reveal that compared with the mono-phase nickel phosphide, the construction of Ni_xP asymmetric structure manipulate the electronic structure and d-band center, promoting the adsorption of intermediates, as well as accelerate phase transition of the OER process. Moreover, the weak adsorption energy of Cl^- on the surface of the Ru-Ni_2P/Ni_5P_4 catalyst avoids the corrosion of Cl^- in seawater. Consequently, Ru-Ni_2P/Ni_5P_4 achieve 1000 mA cm^{-2} with overpotentials of only 128 and 450 mV for HER and OER, respectively. After assembling the Anion-exchange-membrane water electrolyzer (AEMWE), Ru-Ni_2P/Ni_5P_4 shows high average efficiency and economic value at different current densities, and demonstrates its corrosion resistance to Cl^- and potential for industrial applications.

1. Introduction

Hydrogen, as an important product of converting renewable energy into clean energy, is an important part of achieving the dual-carbon goal and building a clean energy system [1–3]. Electrochemical water splitting is a safe and efficient way to produce hydrogen. Nevertheless, seawater resources, which are more abundant than pure water resources, have attracted more widespread attention [4–6]. However, seawater contains a large amount of Cl^-, and the thermodynamic similarity between the oxygen evolution reaction (OER) and the chlorine oxidation reaction (ClOR) leads to the production of ClO^-, which severely corrodes the catalyst, weakening its activity and durability [7–9]. Currently, noble metal catalysts such as RuO_2 and Pt/C have exhibited high efficiencies in both OER and hydrogen evolution reactions (HER), however, its large-scale application is limited by scarcity and high cost [9,10]. Therefore, achieving high current densities at low voltages while developing bifunctional catalysts is a top priority [11].

In recent years, transition metal phosphides (TMPs) have attracted much attention as bifunctional catalysts, and it is noteworthy that due to the high electronegativity of the P atoms in the TMPs, they can be used as a moiety to capture positively charged protons, thus providing high activity for the desorption of H_2 [12,13]. In contrast to the traditional symmetric structure, the electronic structure of the catalysts can be modulated by rationally constructing the asymmetric coordination structure [14–16]. Wang et al. [17]. prepared asymmetric Janus heterostructure of CeO_2/ZnCoS (J−CeO_2/ZCS) through a heterogeneous interfacial induction strategy, which owns the ability to efficiently

* Corresponding author at: Key Laboratory of Eco-chemical Engineering, Ministry of Education, International Science and Technology Cooperation Base of Eco-chemical Engineering and Green Manufacturing, College of Chemical Engineering, Qingdao University of Science and Technology, Qingdao 266042, PR China.
** Corresponding author.
E-mail addresses: chijingqi@qust.edu.cn (J. Chi), inorchemwl@126.com (L. Wang).

https://doi.org/10.1016/j.apcatb.2024.123995
Received 18 January 2024; Received in revised form 7 March 2024; Accepted 20 March 2024
Available online 21 March 2024

regulate the electronic structure and charge redistribution, thereby enhancing the redox activity of the active site and the uptake/desorption of reaction intermediates. Therefore, utilizing the asymmetric coordination to modulate the electronic structure of phosphides at the interface may be an effective strategy to facilitate the seawater electrolysis [18–20]. For HER, the H* adsorption strength is considered to be an intuitive indicator for evaluating the performance of HER, and the electron cloud density near the d-orbitals as well as the position of the d-band center affect the HER performance of the catalyst [21–24]. For OER, by adjusting the charge distribution at the phosphides interface, a phase transition can occur at low voltage, thus serving as a true active site to accelerate the OER kinetics [25,26]. However, utilizing the asymmetric coordination to manipulate electronic structure of phosphides as bifunctional electrocatalysts for seawater electrolysis is barely reported and the reaction mechanisms and dynamic evolution of the HER and OER, particularly concerning the asymmetric coordination to enhance the corrosion-resistance of seawater electrolysis is even less reported [27,28].

Based on the above-mentioned, Ru-doped nickel phosphide asymmetric structure (Ru-Ni_2P/Ni_5P_4) has been synthesized, exhibiting an excellent bifunctional performance for alkaline seawater electrolysis. In-situ characterization technique and DFT calculations reveal that compared with the monophase nickel phosphide, the construction of Ni_xP asymmetric structure manipulate the electronic structure and d-band center, promoting the adsorption of intermediates, as well as accelerate phase transition of the OER process and decrease the adsorption of Cl^- [29,30]. As a result, Ru-Ni_2P/Ni_5P_4 achieve 1000 mA cm^{-2} with overpotentials of only 128 and 450 mV for HER and OER in alkaline seawater, respectively. After assembling the anion-exchange membrane water electrolyzer (AEMWE),

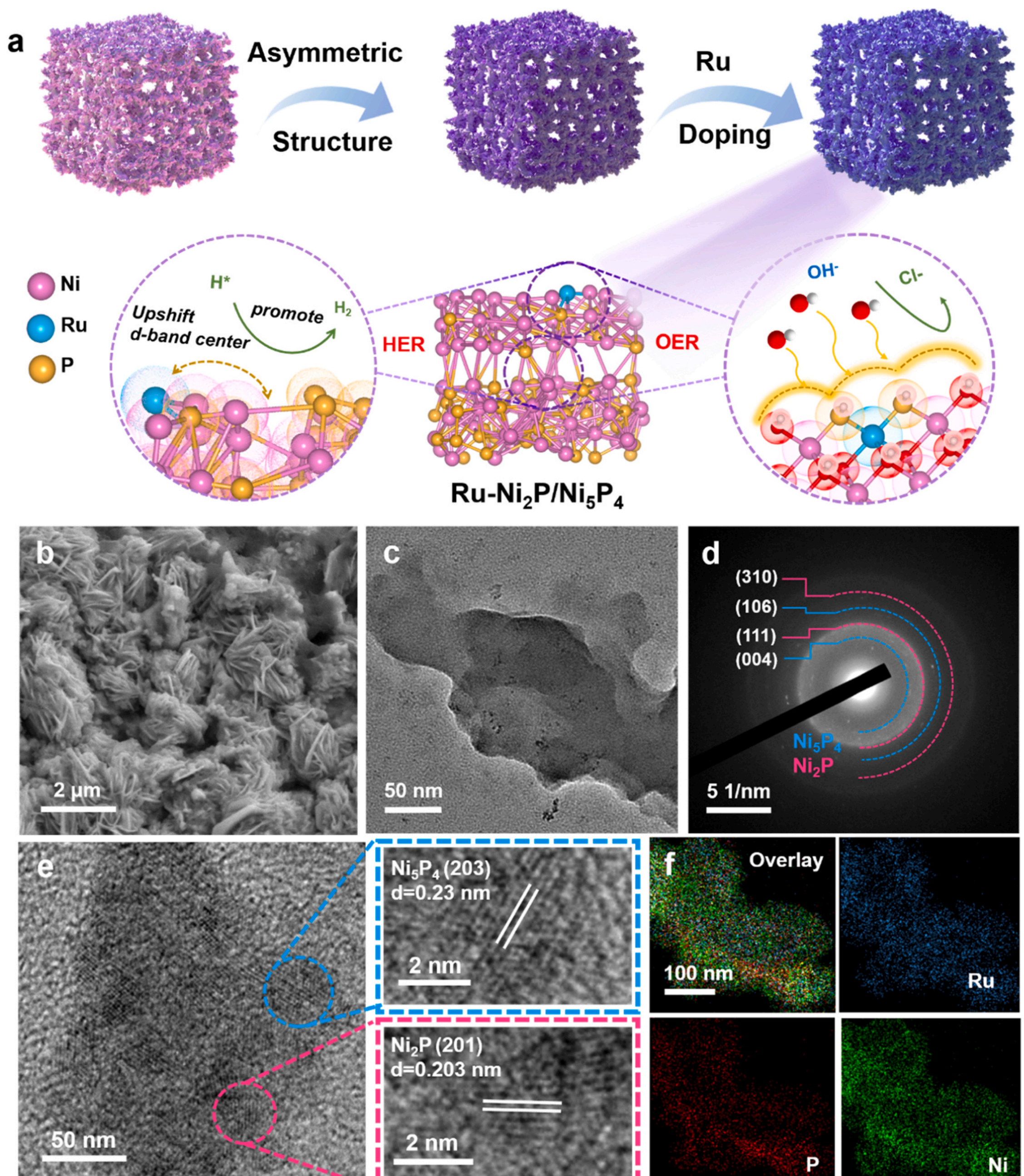

Fig. 1. (a). Schematic diagram of the preparation process for Ru-Ni_2P/Ni_5P_4. (b) SEM, (c) TEM, (d) typical SAED pattern, and (e) HRTEM images of Ru-Ni_2P/Ni_5P_4. (f) TEM mapping image of Ru-Ni_2P/Ni_5P_4.

Ru-Ni_2P/Ni_5P_4 exhibits an average efficiency of approximately 67% at different current densities, high energy intensity and low price of per GGE H_2 produced. The stability of the catalyst is demonstrated for more than 120 h at 500 mA cm^{-2}, proving its excellent resistance to Cl^- corrosion and showing its potential for industrial applications.

2. Result and discussion

2.1. Synthesis and characterization of Ru-Ni_2P/Ni_5P_4

Ru-doped Ni_5P_4/Ni_2P heterojunction structures were synthesized with abundant and dense nanosheet-like morphology through a fast molten salt and low-temperature phosphating strategy (Fig. 1a). The nickel foam (NF) with smooth surface and high electrical conductivity is used as support substrate (Fig. S1a). Firstly, the $Ni_2(NO_3)_2(OH)_2{\cdot}2\,H_2O$ (NiNOOH) with uniform nanosheet-like structure is in-situ grown on NF by a fast molten salt strategy (Fig. S1b). Afterwards, the Ni_2P/Ni_5P_4 structure was synthesized by means of low-temperature phosphating, and the formation of nanoparticles could be observed by scanning electron microscopy (SEM) (Fig. S1c), in which the formation of single or two phases of nickel phosphide could be realized by varying the phosphating time. Finally, doping of Ru elements in different concentrations of $RuCl_3$ solution (Ru-Ni_2P/Ni_5P_4-x, x=0.01, 0.05, 0,1), the formation of abundant and dense nanoparticles on nanosheets are observed (Fig. 1b). Transmission electron microscopy (TEM) images of Ru-Ni_2P/Ni_5P_4 further showed that the surface of Ru-Ni_2P/Ni_5P_4 is consisted of a large number of nanosheets with a homogeneous distribution (Fig. 1c). The formation of Ni_2P and Ni_5P_4 phases is further demonstrated by selective electron diffraction (SAED) pattern (Fig. 1d). Phosphating promotes the formation of the Ni_xP asymmetric structure and further high-resolution TEM (HRTEM) analysis reveal a spacing of 0.203 nm attributed to the (201) crystal plane Ni_2P (Fig. 1e), whereas a spacing of 0.23 nm is attributed to the (203) crystal plane Ni_5P_4, evidencing the formation of a heterogeneous interface. To further verify the composition and elemental distribution of the Ru-Ni_2P/Ni_5P_4 nanosheets, the energy-dispersive X-ray spectroscopy (EDX) elemental mappings analysis indicates that the elements of Ru, Ni, and P are uniformly distributed throughout the nanosheets without any obvious

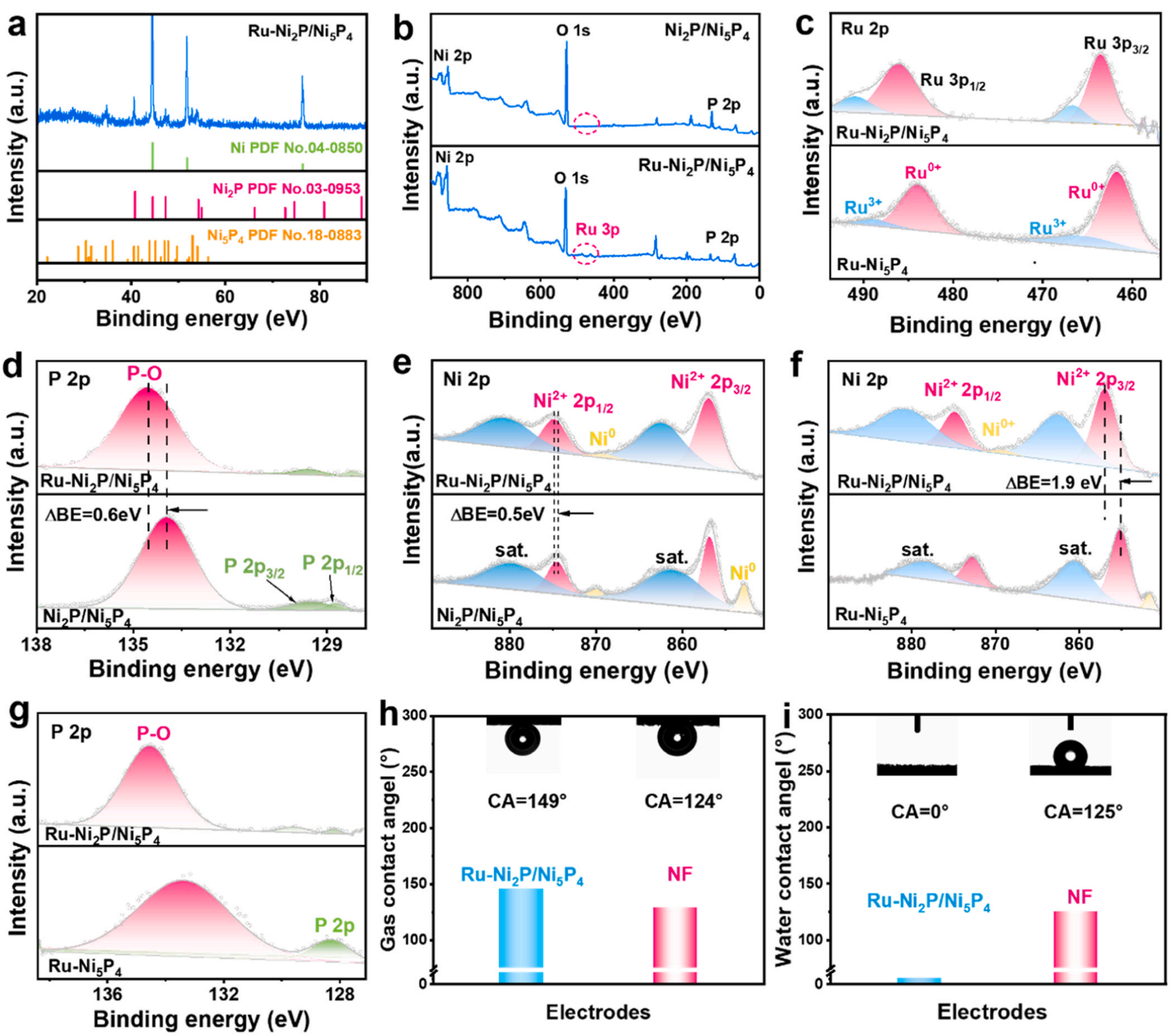

Fig. 2. (a) XRD pattern and (b) XPS survey spectra. High-resolution XPS spectra of (c) Ru 2p, (d, g) P 2p, (e, f) Ni 2p for as-prepared samples. (h, i) Photographs of contact angle measurements of Ru-Ni_2P/Ni_5P_4 and NF.

aggregation (Fig. 1f), which prove the homogeneous doping of Ru elements. The content of Ru in the nanosheets is determined using ICP-AES, and the content of Ru is only 2.28 wt% (Table S1), which is much lower than the weight percentage of commercial Pt/C and RuO_2 catalysts.

As shown in Fig. S2, the peaks of Ni_2P (JCPDS No.89–4864) and Ni_5P_4 (JCPDS No.84–2588) are shown in X-ray diffraction (XRD) after low-temperature phosphating prior to immersion in $RuCl_3$ solution, indicating the synthesis of the Ni_2P/Ni_5P_4 asymmetric structure. Fig. 2a confirms that XRD pattern of Ru-Ni_2P/Ni_5P_4 samples match well with the standard Ni_2P (JCPDS No.03–0953) and the standard Ni_5P_4 (JCPDS No.18–0883) and no phase of Ru monomers is observed, suggesting that the Ru element is in the doped form into the asymmetric structure. The XRD of the samples synthesized from molten salt corresponds to Ni $(NO_3)_2(OH)_2$ 2 H_2O (NiNOOH) (JCPDS No. 00–027–0939) (Fig. S3). In order to investigate the electronic interactions of the Ru-Ni_2P/Ni_5P_4 catalyst, X-ray photoelectron spectroscopy (XPS) was performed. As can be seen from the comparative XPS spectra in Fig. 2b, Ru element is successfully introduced in Ru-Ni_2P/Ni_5P_4, both Ni_2P/Ni_5P_4 and Ru-Ni_2P/Ni_5P_4 catalysts indicate the existence of Ru, Ni and P elements. As shown in Fig. 2c, peaks at 486 and 463.4 eV in the Ru 3p spectrum of Ru-Ni_2P/Ni_5P_4 are attributed to the Ru $3p_{3/2}$ and Ru $3p_{1/2}$ of Ru^0, and the peaks at 490.8 and 466.4 eV are two peaks of Ru^{3+} [31,32]. Moreover, comparing the peaks of Ru 2p of Ru-Ni_2P/Ni_5P_4 with Ru-Ni_5P_4, it can be seen that Ru 2p of Ru-Ni_2P/Ni_5P_4 is shifted towards higher binding energy, suggesting that more electrons are transferred towards the asymmetric structure interface. For Fig. 2d, the fitted peaks corresponding to 134.5 and 133.9 eV indicate the presence of P-O bonds in Ru-Ni_2P/Ni_5P_4 and Ni_2P/Ni_5P_4, and the other two peaks located near 129.5 eV are attributable to the $2p_{1/2}$ and $2p_{3/2}$ of M-P [33,34]. Fig. 2e shows the high-resolution XPS spectra of Ni can be divided into five main peaks. Peaks at 874.8 and 862.5 eV belong to the $2p_{1/2}$ and $2p_{3/2}$ orbitals of Ni^{2+}, peaks at 880.7 and 869.1 eV belong to the satellite peaks, and peaks at 869.1 eV belongs to Ni^0 [35]. Therefore, comparing the XPS of the two catalysts for Ni 2p and P 2p spectra of both Ni 2p and P 2p orbitals, the doping of Ru result in an overall shift of the peaks of both Ni 2p and P 2p orbitals towards higher binding energies, suggesting that the doping of Ru change the electronic environment at the Ni_2P/-Ni_5P_4 asymmetric heterointerface [36]. To further explore the effect of constructing asymmetric structure on the catalyst, the XPS of Ni 2p and P 2p of Ru-Ni_2P/Ni_5P_4 and Ru-Ni_5P_4 are compared (Figs. 2f and 2g) and Ru-Ni_2P/Ni_5P_4 with asymmetric structure shift towards higher binding energies, suggesting that Ru doping in Ni_xP asymmetric structure has a more pronounced electron-transfer process. In order to demonstrate the superiority of the Ru-Ni_2P/Ni_5P_4 catalyst, contact angle tests (CA) were performed. Firstly, the contact angle test with water is compared, and when the water droplets are contacted with the Ru-Ni_2P/Ni_5P_4, they are rapidly penetrated with a contact angle close to 0°, proving the super hydrophilicity of the catalyst. By contrast, the smooth surface NF without catalyst nanosheets loading show poorer hydrophilicity with a CA of 125° (Fig. 2h). Moreover, gas bubble CA tests indicate that Ru-Ni_2P/Ni_5P_4 and pure NF have CA of 149° and 124°, respectively, and Ru-Ni_2P/Ni_5P_4 exhibits superior gas transport performance (Fig. 2i). The unique nanosheets morphology of Ru-Ni_2P/Ni_5P_4 contributes to surface wettability and bubble release during water electrolysis [37]. Thus, the hydrophilic gas-transport characteristic of Ru-Ni_2P/Ni_5P_4 nanosheets can accelerate water dissociation and bubbles diffusion, which is conducive to the seawater electrolysis.

2.2. Electrocatalytic performance of Ru-Ni_2P/Ni_5P_4 investigation for HER and OER

The catalytic activities of Ru-Ni_2P/Ni_5P_4-x (x=0.01, 0.05, 0.1) with different Ru loading was firstly investigated in a typical three-electrode system (Fig. S4a and S4b). By comparing the catalysts with different Ru contents, it can be seen that the Ru content of 5 mg mL^{-1} concentration is the optimal choice after the comprehensive performance and economic value considerations. Based on that, The Ru content of 5 mg mL^{-1} was selected for subsequent tests. In order to investigate the effects of asymmetric Ni_xP structure as well as Ru doping on the catalyst performance, LSV curves of Ru-Ni_2P/Ni_5P_4, Ru-Ni_5P_4 and commercial Pt/C and RuO_2 performances were compared under the same conditions (Fig. 3a). Apparently, Ru-Ni_2P/Ni_5P_4 exhibits excellent HER and OER performance, and the LSV curves show that low overpotentials of only 128 and 450 mV are required to achieve high current density at 1000 mA cm^{-2} for HER and OER, respectively, much smaller than the overpotentials of Ru-Ni_5P_4 (200 and 604 mV), the benchmark commercial Pt/C (227 mV) and RuO_2 (470 mV) (Fig. 3b). The Tafel slopes of different catalysts show that the Ru-Ni_2P/Ni_5P_4 nanosheets exhibit the smallest Tafel slopes in HER and OER (52 and 51 mV dec^{-1}), respectively, which are even lower than those of commercial Pt/C and RuO_2 (71 and 74 mV dec^{-1}), indicating that the Ru-Ni_2P/Ni_5P_4 electrode display fast HER and OER kinetics (Fig. S5a and S5b). Based on electrochemical impedance spectroscopy (EIS) measurements, the Ru-Ni_2P/Ni_5P_4 electrode exhibit the smallest semicircle and the lowest charge transfer resistance (R_{ct}) values in the low frequency range compared with the control sample (Fig. S6a and S6b), suggesting a fast charge transfer resistance within the Ru-Ni_2P/Ni_5P_4 catalyst, which is consistent with the LSV curves and Tafel slopes. The Ru-Ni_2P/Ni_5P_4 nanosheets have excellent activity, which is well ahead of the recently reported bifunctional HER and OER catalysts (Fig. 3c and Table S2). In addition, we obtain cyclic voltammogram curves with different scan rates at non-Faraday region (Fig. S7-S8), and then fit the double layer capacitance (C_{dl}), as shown in Fig. S9. It can be found that the Ru-Ni_2P/Ni_5P_4 exhibits the largest C_{dl} value, which further reflects that the Ru-Ni_2P/Ni_5P_4 can provide more active sites. Fig. 3d summarize the combined comparison of the HER and OER performance of Ru-Ni_2P/Ni_5P_4 with that of Ni_2P/Ni_5P_4 and Ru-Ni_5P_4 based on the above mentioned tests, suggesting that Ni_xP asymmetric structure with Ru doping improve the HER and OER performance.

Moreover, the HER and OER performance of the catalysts in different alkaline solutions were tested in simulated seawater (1.0 M KOH + 0.5 M NaCl) and real seawater (1.0 M KOH + seawater). As shown in Fig. S10-S15, the LSV, Tafel slope, EIS and C_{dl} performance is compared in simulated seawater and real seawater, respectively, and find that its performance in seawater is not much different from that in KOH, thus proving the corrosion resistance to Cl^- during seawater electrolysis.

It is well known that tertiary butyl alcohol (TBA) is a special hydrogen radical eradicator, which is an effective method to study the strength of hydrogen adsorption. As shown in Fig. S16, the HER performance of Ru-Ni_2P/Ni_5P_4 and Ru-Ni_5P_4 is significantly decreased by the addition of 1.0 M TBA, in which the current density of Ru-Ni_5P_4 decrease more significantly, and the overpotentials of Ru-Ni_2P/Ni_5P_4 at 400, 600, and 800 mA cm^{-2} are 2.54, 2.21, and 2.04 times higher than those of Ru-Ni_5P_4, which means that Ru-Ni_5P_4 is more susceptible to the TBA bursting agent, indicating that the asymmetric structure surface has more H* as well as stronger hydrogen adsorption strength (Fig. 3e), which is beneficial to improve the HER process [38,39]. The charge transfer kinetics of the inner layer of the electrode material can be reflected by monitoring the charge transfer resistance (R_{ct}) and double layer capacitance (CPE_1) in the first parallel assembly. A second parallel circuit was preferred to be analysed to truly reflect the charge relaxation behavior of the HER intermediates (Figure S17). Concretely, the adsorption behavior of hydrogen intermediates on chemically active sites can be reflected by fitting the R_{ct} and hydrogen adsorption pseudo capacitance (C_φ) (Fig. 3f). It is not difficult to see that the hydrogen adsorption charge (Q_{H^*}) calculated by integrating the processed C_φ is greatly improved for Ru-Ni_2P/Ni_5P_4 compared with the Q_{H^*} of Ru-Ni_5P_4, which is sufficient to prove that the Ni_xP asymmetric structure greatly improves the H* adsorption strength on Ru-Ni_2P/Ni_5P_4 [40]. In order to demonstrate that Ru-Ni_2P/Ni_5P_4 has a better OH* adsorption capacity than Ru-Ni_5P_4, the tests were carried out in KOH-H_2O and KOH-D_2O electrolytes respectively. The presence of a stronger deuterium bonding

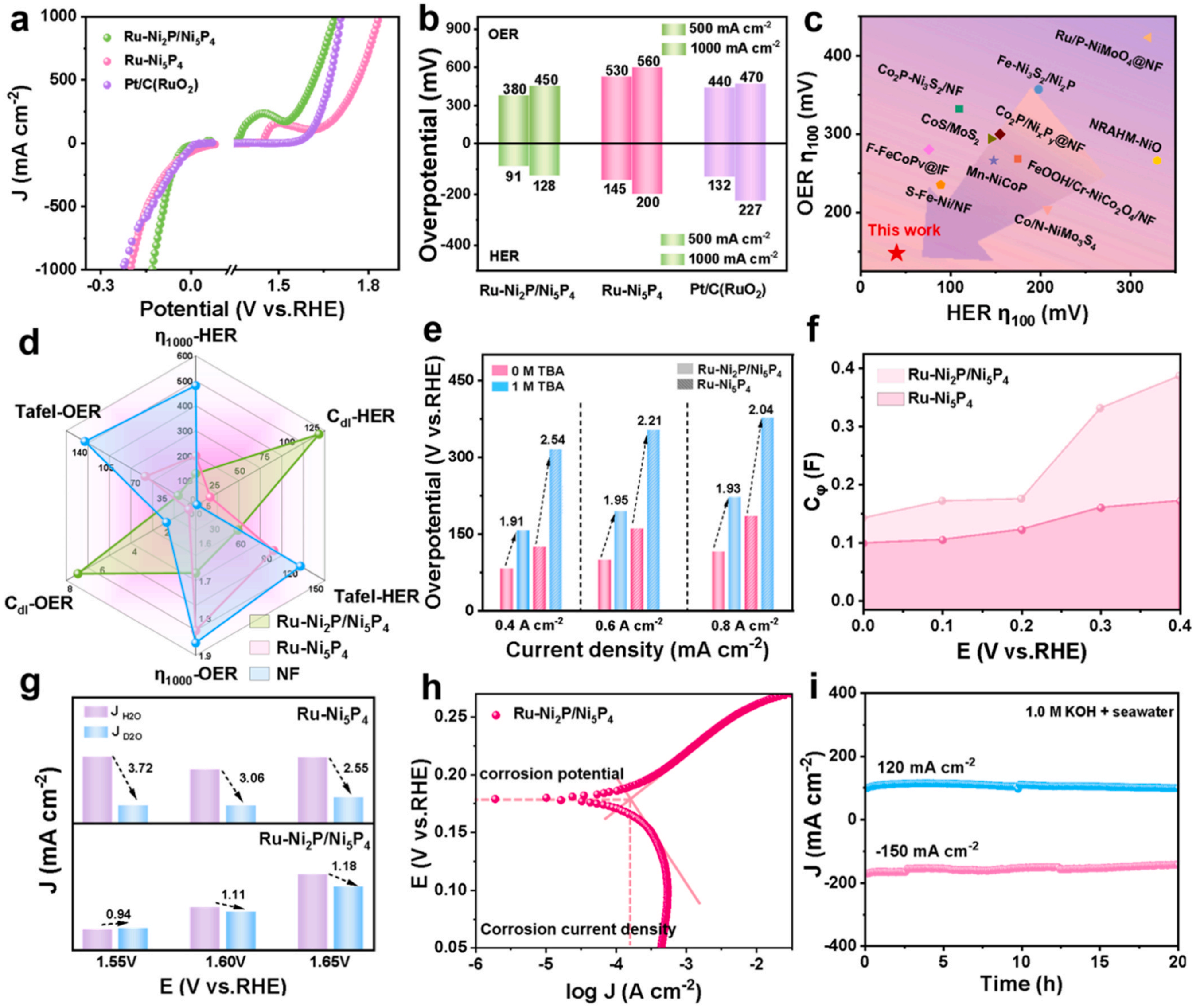

Fig. 3. (a) LSV performance of different samples and (b) corresponding HER and OER overpotentials at different current density. (c) Comparison of the overpotential for HER and OER with other electrocatalysts. (d) Comprehensive comparisons of the HER and OER performance. (e) The overpotentials at different current density of Ru-Ni_2P/Ni_5P_4 with other samples in 1.0 M KOH with and without TBA. (f) Plots of C_φ vs η during HER, (g) OER kinetics investigations, and (h) Tafel plots of Ru-Ni_2P/Ni_5P_4 in 1.0 M KOH + seawater. (i) Chronoamperometry i-t curve of Ru-Ni_2P/Ni_5P_4 for HER and OER.

network in D_2O than the O-H in H_2O, and the fact that the O-D bonds in D_2O are more difficult to break during catalysis due to their stronger bonding energy than the O-H bonds. Therefore, the OER overpotential of Ru-Ni_2P/Ni_5P_4 occurring in KOH-D_2O increases relative to that of KOH-H_2O (Fig. S18). In addition, it was proved by calculation that Ru-Ni_2P/Ni_5P_4 has stronger adsorption of OH^-. Therefore, in D_2O, the smaller the decay, the stronger the adsorption of OH* is proved and the smaller the overpotential is required (Fig. 3g) [41]. In particular, due to the formation of ClO^- corrosion by Cl^- oxidation during the OER process, we test two samples for their resistance to Cl^- corrosion [42], and it is clear that Ru-Ni_2P/Ni_5P_4 has higher corrosion potential, which indicates its excellent corrosion resistance (Fig. 3h and S19).

In considering the practical application of catalysts, durability is an important factor. As shown in Fig. 3i, in alkaline seawater, the Ru-Ni_2P/Ni_5P_4 catalyst shows negligible current attenuation after sustained electrolysis for 20 h at about 120 and 150 mA cm^{-2}, respectively, suggesting that the Ru-Ni_2P/Ni_5P_4 has excellent stability. After stability testing, TEM and XPS of Ru-Ni_2P/Ni_5P_4 were further determined. As shown in Fig. S20, it can be clearly observed that the catalyst maintains the nanosheet-like structure after HER and the formation of the amorphous layer can be clearly observed in TEM after the stabilization of OER due to the anodic oxidation reaction. From the XPS spectra of Ni 2p (Fig. S21), it can be observed that a new peak appeared at 865.1 and 881.4 eV belong to the peak of Ni^{3+}, indicating the generation of NiOOH during the OER process. And the peak of PO_4^{3-} appearing in the P 2p spectrum carries an anionic charge that has a homogeneous repulsion with Cl^-, thus greatly avoiding the corrosion of the catalyst. As shown in Fig. S22, the nearly unchanged peaks of the Ni 2p, P 2p, and Ru 2p spectra in the XPS after HER demonstrates that no phase transition occurs during the HER process. In addition, we further detected the generation of ClO^- in the electrolyte after the OER reaction by a colourimetric method. When free chlorine is present, N, N-diethyl-p-phenylenediamine sulphate reacts to form a red dye with strong absorption. Therefore, it was measured by UV–vis spectrophotometer (Fig. S23). As shown in Fig. S24, no ClO^- was generated after the OER reaction, indicating that no chlorine gas was produced as a by-product [43].

2.3. Mechanism of improving HER and OER performance of Ru-Ni_2P/Ni_5P_4

For the possible changes in the HER and OER processes, we tested the possible phase transitions in the HER and OER processes by in-situ Raman. Fig. 4a demonstrates the Raman comparison of Ru-Ni_2P/Ni_5P_4 and Ru-Ni_5P_4 in the HER voltage range, respectively, and neither of them shows the generation of new phases in the HER voltage range, and only Ni-P bonds can be indicated, which proves that the phase transition does not occur in the HER process. For the OER process, since the transition metal catalyst undergoes an irreversible phase transition process during the OER process, and thus the oxyhydroxide generated on the surface of the catalyst are considered to be the real active sites in the OER process. Therefore, the in-situ Raman of Ru-Ni_2P/Ni_5P_4 and Ru-Ni_5P_4 under OER conditions are shown in Figs. 4b and 4c, respectively, and it can be clearly observed that the peaks of NiOOH in Ru-Ni_2P/Ni_5P_4 appear at a voltage of 1.45 V, whereas those of NiOOH in Ru-Ni_5P_4 appear at 1.55 V, indicating that the construction of Ni_2P/Ni_5P_4 asymmetric structure in the OER process could accelerate the formation of NiOOH as the OER active sites [44,45]. Subsequently, the theoretical model of Ru-Ni_2P/Ni_5P_4, Ru-Ni_5P_4, Ru/P-NiOOH were constructed (Fig. S25). As shown in Fig. S26, when Ru atom is doped, it causes a change in the charge density around the Ni and P atoms near the Ru atom. In addition, we also compare the charge changes when the Ru element is doped in Ni_5P_4 monophase and Ni_2P/Ni_5P_4 asymmetric structure. Undoubtedly, Ru transfers more electrons (0.079 e) to the Ni_xP asymmetric structure, which contributes to the excitation of Ni_xP activity. The total density of states (TDOS) of Ru-Ni_2P/Ni_5P_4 and Ru-Ni_5P_4 were further calculated (Fig. 4d), and the comparison reveal that Ru-Ni_2P/Ni_5P_4 has the highest charge density near the Fermi energy level, suggesting an enhanced conductivity. Moreover, comparing the d-band center of Ru-Ni_5P_4 (-1.23 V), the d-band center of Ru-Ni_2P/Ni_5P_4 (-1.19 V) is closer to the Fermi energy level, suggesting that the Ru doping and Ni_2P/Ni_5P_4 asymmetric structure facilitate the adsorption of intermediates during the reaction process and enhances the electrochemical process. Furthermore, Ru-Ni_2P/Ni_5P_4 has the lowest work

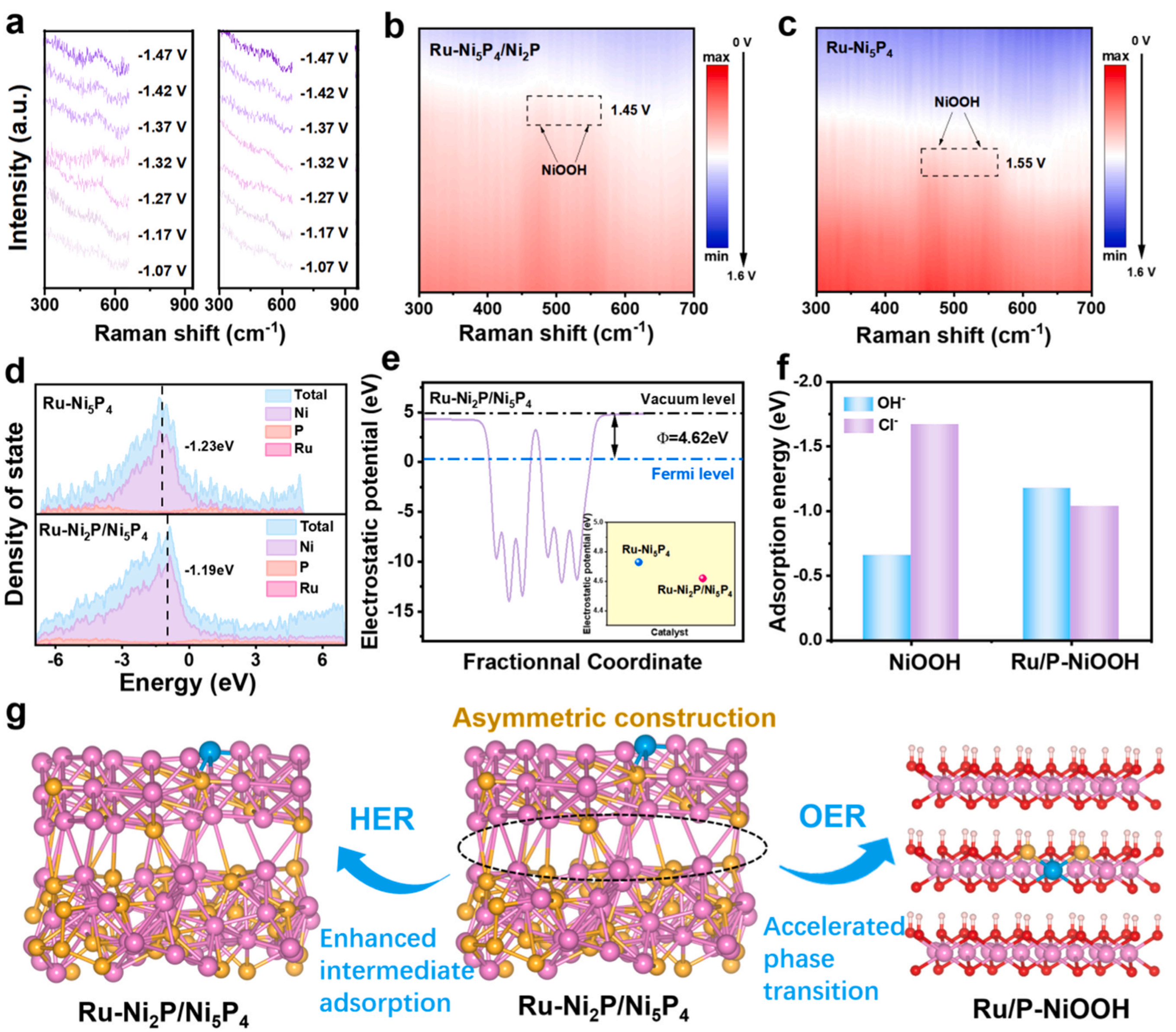

Fig. 4. In-situ Raman for (a) Ru-Ni_2P/Ni_5P_4 and Ru-Ni_5P_4 in HER. In-situ Raman of (b) Ru-Ni_2P/Ni_5P_4 and (c) Ru-Ni_5P_4 in OER. (d) DOS of Ru-Ni_2P/Ni_5P_4, Ru-Ni_5P_4 and Ni_2P/Ni_5P_4. (e) The computed work functions of Ru-Ni_2P/Ni_5P_4. (f) Comparison of Cl^- and OH^- adsorption energies for NiOOH and Ru/P-NiOOH. (g) Schematic representation of the genuine phases and active sites of Ru-Ni_2P/Ni_5P_4 in 1.0 M KOH seawater during HER and OER.

function (4.62 eV), which is lower than that of Ru-Ni_5P_4 (5.14 eV) (Fig. 4e and S27), suggesting that electrons are more likely to spill over from the interior of Ru-Ni_2P/Ni_5P_4 to the surface and exchange electrons with the reactants, thus better accelerating the electrocatalytic dynamic process. In addition, the adsorption energy of OH^- from seawater by Ru/P-NiOOH in the OER process is higher than that of Cl^-, thus demonstrating the excellent Cl^- repellency in the OER process (Fig. 4f). In conclusion, the introduction of Ni_2P/Ni_5P_4 asymmetric structure in Ru-Ni_2P/Ni_5P_4 promotes the adsorption of intermediates in HER process, also facilitates the electron transfer and fast phase transition in OER process, and repels Cl^- simultaneously, which is conducive to the efficient and stable overall seawater electrolysis (Fig. 4g).

2.4. Investigation of electrocatalytic activity for overall seawater splitting

Based on the revelation of the excellent bifunctional catalytic activity of Ru-Ni_2P/Ni_5P_4 catalysts in alkaline seawater, the activity of Ru-Ni_2P/Ni_5P_4 in a two-electrode electrolyzer by simulating industrial electrolysis conditions in 1.0 M KOH + seawater solutions was tested and compared it with commercial Pt/C and RuO_2. As shown in Fig. 5a, it can be observed that the comparison of the LSV curves reveals that the performance of Ru-Ni_2P/Ni_5P_4 couple in seawater is much better than that of commercial Pt/C and RuO_2. In 1.0 M KOH + seawater, the voltage required for a large current density of 1000 mA cm^{-2} is only 1.83 V, which is much smaller than that of commercial Pt/C and RuO_2 (2.09 V). Significantly, the performance of Ru-Ni_2P/Ni_5P_4||Ru-Ni_2P/Ni_5P_4 barely exceeds that of the most recorded catalysts (Fig. 5b, Tables S3 and S4). In addition, when the chronoamperometry i-t curve is measured in 1.0 M KOH + seawater, it can last for 100 h at a current density of 100 mA cm^{-2} almost no degradation (Fig. 5c). Subsequently, calculated Faraday efficiency by collecting hydrogen from the cathode and oxygen from the anode in 1.0 M KOH + seawater based on the drainage method, where bubbles were produced at both the cathode and anode of the electrolyzer, which could be reflected by the decrease of the

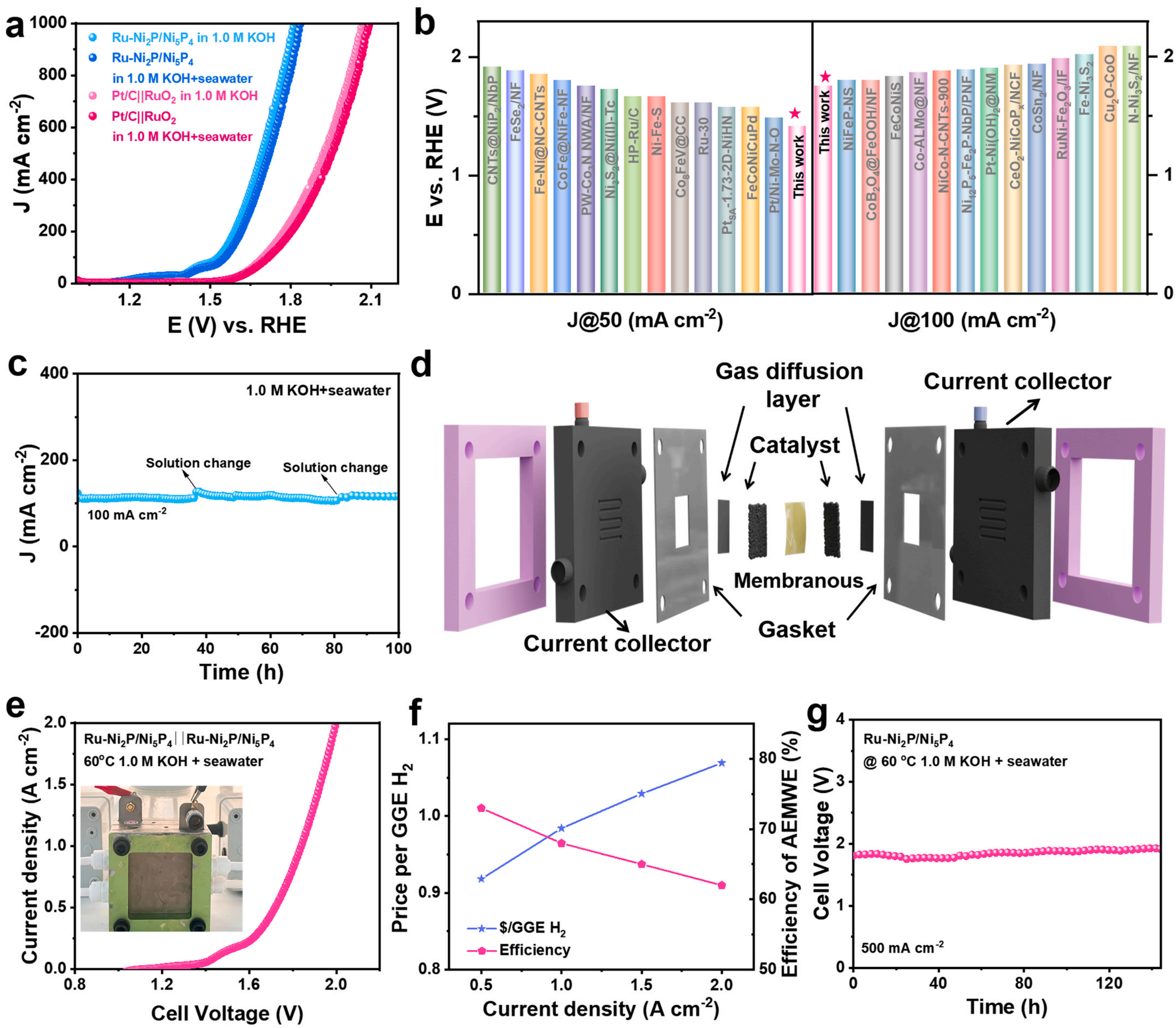

Fig. 5. (a) LSV curves in different solutions for overall seawater splitting. (b) Comparison of operation voltages required to achieve 50 and 100 mA cm^{-2} with benchmarking works. (c) Chronoamperometry curve of Ru-Ni_2P/Ni_5P_4 in 1.0 M KOH seawater. (d) Schematic diagram of the AEMWE electrolyzer. (e) Polarization curves of Ru-Ni_2P/Ni_5P_4||Ru-Ni_2P/Ni_5P_4 electrodes, the inset is a picture of the AEMWE device. (f) Efficiency of AEMWE electrolyzer at different current densities and price of per GGE H_2. (g) Chronopotentiometry curve of Ru-Ni_2P/Ni_5P_4||Ru-Ni_2P/Ni_5P_4 at 500 mA cm^{-2}.

solution in the test tube. As shown in Fig. S28, the obtained V_{H2}/V_{O2} value is calculated to be 2:1, thus inferring that the catalyst has a Faraday efficiency close to 100% in 1.0 M KOH + seawater. The overall seawater electrolysis process can then be driven by a stirling engine (Fig. S29a), and bubble generation on the catalyst surface can be clearly observed. In addition, HER and OER bifunctional performance of the Ru-Ni_2P/Ni_5P_4 electrocatalyst can be demonstrated based on the energy supplied by the solar panel (Fig. S29b), which can be accomplished with only 1.82 V to achieve 130 mA cm^{-2}, further proving that the Ru-Ni_2P/Ni_5P_4 catalyst has obvious potential for seawater electrolysis. In order to verify its potential for industrial application, Ru-Ni_2P/Ni_5P_4 was assembled as cathode and anode in an AEMWE to test its performance. Fig. 5d shows the schematic of the AEMWE device, and we subsequently simulate the industrial conditions of 60 °C seawater for testing, as shown in Fig. 5e, where a high current density of 1000 mA cm^{-2} can be achieved at a voltage of only 1.83 V. In addition, we evaluate the economic viability of the AEM electrolyzer with an average efficiency of AEMWE is approximately 67% at different current densities and a price of per gasoline-gallon equivalent (GGE) H_2 of $1 [42], far below the U.S. Department of Energy's price standard of $2 in 2026 (Fig. 5f). In order to verify the stability of the Ru-Ni_2P/Ni_5P_4 catalysts in AEMWE, long-term stability tests were subsequently performed under simulated industrial conditions. As shown in Fig. 5g, the Ru-Ni_2P/Ni_5P_4 catalyst is able to operate stably at a current density of 500 mA cm^{-2} for more than 120 h without significant voltage drop.

3. Conclusion

In this work, bifunctional Ru-doped Ni_xP asymmetric electrocatalysts (Ru-Ni_2P/Ni_5P_4) for alkaline seawater-based anionic membrane (AEM) electrolyzer has been prepared. In situ characterizations and theoretical calculations show that the introduction of asymmetric structure manipulate the electronic structure and d-band center of Ru-Ni_2P/Ni_5P_4 and optimize the adsorption of the active site for H*, resulting in an enhanced HER activity. Moreover, the introduction of the asymmetric structure lead to a rapid phase transition of Ru-Ni_2P/Ni_5P_4 into real oxyhydroxide active species. The co-doping of Ru/P elements modulate the adsorption energies of Cl^- and OH^-, enhancing the selectivity of OH^- by suppressing the erosion of Cl^-, thus ensuring the long cycle stability of the Ru-Ni_2P/Ni_5P_4 for seawater electrolysis. The Ru-Ni_2P/Ni_5P_4 integrated as both cathode and anode in an alkaline seawater AEMWE is able to operate continuously for more than 100 h at a high current density of 500 mA cm^{-2} and show great economics. This work has led to the design of asymmetric electrocatalyst with high activity, stability and selectivity for industrial seawater electrolysis.

CRediT authorship contribution statement

Yanan Xia: Investigation, Data curation, Conceptualization, Formal analysis, Validation, Writing-original draft. Conceptualization, Writing-review & editing, Supervision. **Lili Guo:** Formal analysis, Data curation, Conceptualization, Validation. **Jiawei Zhu:** Supervision, Formal analysis, Data curation. **Junheng Tang:** Data curation, Conceptualization, Validation. **Zhipeng Li:** Conceptualization, Validation. **Xiaobin Liu:** Supervision, Validation, Conceptualization. **Jingqi Chi:** Supervision, Validation, Funding acquisition. **Lei Wang:** Writing-review & editing, Funding acquisition, Supervision.

Declaration of Competing Interest

The authors declare that they have no known competing financial interests or personal relationships that could have appeared to influence the work reported in this paper.

Data Availability

The data that has been used is confidential.

Acknowledgements

This work is financially supported from the National Natural Science Foundation of China (52072197, 52174283, and 22301156), the Natural Science Foundation of Shandong Province (ZR2021QE165), Youth Innovation and Technology Foundation of Shandong Higher Education Institutions, China (2019KJC004), Major Scientific and Technological Innovation Project (2019JZZY020405), Major Basic Research Program of Natural Science Foundation of Shandong Province under Grant (ZR2020ZD09), Shandong Province "Double-Hundred Talent Plan" (WST2020003), Taishan Scholar Young Talent Program (tsqn201909114), and University Youth Innovation Team of Shandong Province (202201010318).

Appendix A. Supporting information

Supplementary data associated with this article can be found in the online version at doi:10.1016/j.apcatb.2024.123995.

References

[1] J. Chang, G. Wang, Z. Yang, B. Li, Q. Wang, R. Kuliiev, N. Orlovskaya, M. Gu, Y. Du, G. Wang, Y. Yang, Dual-doping and synergism toward high-performance seawater electrolysis, Adv. Mater. 33 (2021) 2101425.

[2] J. Liang, Z. Li, X. He, Y. Luo, D. Zheng, Y. Wang, T. Li, B. Ying, S. Sun, Z. Cai, Q. Liu, B. Tang, X. Sun, Electrocatalytic seawater splitting: nice designs, advanced strategies, challenges and perspectives, Mater. Today 69 (2023) 193–235.

[3] J. Li, Y. Tan, M. Zhang, W. Gou, S. Zhang, Y. Ma, J. Hu, Y. Qu, Boosting electrocatalytic activity of Ru for acidic hydrogen evolution through hydrogen spillover strategy, ACS Energy Lett. 7 (2022) 1330–1337.

[4] J. Zhu, J. Chi, X. Wang, T. Cui, L. Guo, B. Dong, X. Liu, L. Wang, Boosting hydrogen evolution reaction activity of Ru anchored binary oxyhydroxide by F-doping in alkaline seawater, Nano Energy 121 (2024) 109249.

[5] L. Yu, Q. Zhu, S. Song, B. McElhenny, D. Wang, C. Wu, Z. Qin, J. Bao, Y. Yu, S. Chen, Z. Ren, Non-noble metal-nitride based electrocatalysts for high-performance alkaline seawater electrolysis, Nat. Commun. 10 (2019) 5106.

[6] X. Wang, B. Liu, Y. Zhang, T. Butburee, K. Ostrikov, S. Wang, W. Huang, Development of ABO_4-type photoanodes for photoelectrochemical water splitting, EcoEnergy 1 (2023) 108–153.

[7] H. Liu, W. Shen, H. Jin, J. Xu, P. Xi, J. Dong, Y. Zheng, S.Z. Qiao, High-performance alkaline seawater electrolysis with anomalous chloride promoted oxygen evolution reaction, Angew. Chem. Int. Ed. 62 (2023) e202311674.

[8] D. Jin, H. Woo, S. Prabhakaran, Y. Lee, M.H. Kim, D.H. Kim, C. Lee, Single phase trimetallic spinel $CoCr_xRh_{2-x}O_4$ nanofibers for highly efficient oxygen evolution reaction under freshwater mimicking seawater conditions, Adv. Funct. Mater. 33 (2023) 2301559.

[9] J. Guo, Y. Zheng, Z. Hu, C. Zheng, J. Mao, K. Du, M. Jaroniec, S.-Z. Qiao, T. Ling, Direct seawater electrolysis by adjusting the local reaction environment of a catalyst, Nat. Energy (2023) 264–272.

[10] H. Hu, X. Wang, J.P. Attfield, M. Yang, Metal nitrides for seawater electrolysis, Chem. Soc. Rev. 53 (2024) 163–203.

[11] T.A. Shifa, K. Yusupov, G. Solomon, A. Gradone, R. Mazzaro, E. Cattaruzza, A. Vomiero, In situ-generated oxide in sn-doped nickel phosphide enables ultrafast oxygen evolution, ACS Catal. 11 (2021) 4520–4529.

[12] L. Yu, L. Wu, S. Song, B. McElhenny, F. Zhang, S. Chen, Z. Ren, Hydrogen generation from seawater electrolysis over a sandwich-like NiCoN|Ni_xP|NiCoN microsheet array catalyst, ACS Energy Lett. 5 (2020) 2681–2689.

[13] G.-H. Gao, R.-Z. Zhao, Y.-J. Wang, X. Ma, Y. Li, J. Zhang, J.-S. Li, Core-shell heterostructure engineering of CoP nanowires coupled NiFe LDH nanosheets for highly efficient water/seawater oxidation, Chin. Chem. Lett. (2023) 109181.

[14] X. Wang, X. Zhou, C. Li, H. Yao, C. Zhang, J. Zhou, R. Xu, L. Chu, H. Wang, M. Gu, H. Jiang, M. Huang, Asymmetric $Co\text{-}N_3P_1$ trifunctional catalyst with tailored electronic structures enabling boosted activities and corrosion resistance in an uninterrupted seawater splitting system, Adv. Mater. 34 (2022) 2204021.

[15] W. Xu, H. Tang, H. Gu, H. Xi, P. Wu, B. Liang, Q. Liu, W. Chen, Research progress of asymmetrically coordinated single-atom catalysts for electrocatalytic reactions, J. Mater. Chem. A 10 (2022) 14732–14746.

[16] S.-S. Liu, L.-J. Ma, J.-S. Li, Dual-metal-organic-framework derived CoP/MoP hybrid as an efficient electrocatalyst for acidic and alkaline hydrogen evolution reaction, J. Colloid Interface Sci. 631 (2023) 147–153.

[17] J. Zhang, X. Dong, G. Wang, J. Chen, R. Wang, Interfacial engineering-induced Janus heterostructures with enhanced electronic regulation for efficient oxygen electrocatalysis in rechargeable Zn-air batteries, Appl. Catal. B Environ. 342 (2024) 123459.

[18] X. Li, Z. Kou, S. Xi, W. Zang, T. Yang, L. Zhang, J. Wang, Porous $NiCo_2S_4$/FeOOH nanowire arrays with rich sulfide/hydroxide interfaces enable high OER activity, Nano Energy 78 (2020) 105230.
[19] X. Zheng, H. Nie, Y. Zhan, X. Zhou, H. Duan, Z. Yang, Intermolecular electron modulation by P/O bridging in an IrO_2-CoPi catalyst to enhance the hydrogen evolution reaction, J. Mater. Chem. A 8 (2020) 8273–8280.
[20] M. Wei, L. Huang, L. Li, F. Ai, J. Su, J. Wang, Coordinatively Unsaturated PtCo Flowers Assembled with Ultrathin Nanosheets for Enhanced Oxygen Reduction, ACS Catal. 12 (2022) 6478–6485.
[21] J. Jin, X. Wang, Y. Hu, Z. Zhang, H. Liu, J. Yin, P. Xi, Precisely control relationship between sulfur vacancy and h absorption for boosting hydrogen evolution reaction, Nano-Micro Lett. 16 (2024) 63.
[22] Z. Chen, Y. Song, J. Cai, X. Zheng, D. Han, Y. Wu, Y. Zang, S. Niu, Y. Liu, J. Zhu, X. Liu, G. Wang, Tailoring the d-band centers enables Co_4N nanosheets to be highly active for hydrogen evolution catalysis, Angew. Chem. Int. Ed. 57 (2018) 5076–5080.
[23] Q. Hu, K. Gao, X. Wang, H. Zheng, J. Cao, L. Mi, Q. Huo, H. Yang, J. Liu, C. He, Subnanometric Ru clusters with upshifted D band center improve performance for alkaline hydrogen evolution reaction, Nat. Commun. 13 (2022) 3958.
[24] X.-J. Niu, Y.-J. Wang, G.-H. Gao, T.-D. Yang, J.-W. Mei, Y.-C. Qi, R.-Z. Tian, J.-S. Li, Interfacial engineering of CoP/CoS_2 heterostructure for efficiently electrocatalytic pH-universal hydrogen production, J. Colloid Interface Sci. 652 (2023) 989–996.
[25] X. Liu, J. Chi, H. Mao, L. Wang, Principles of designing electrocatalyst to boost reactivity for seawater splitting, Adv. Energy Mater. 13 (2023) 2301438.
[26] L. Lu, Y. Zhang, Z. Chen, F. Feng, K. Teng, S. Zhang, J. Zhuang, Q. An, Synergistic promotion of HER and OER by alloying ternary Zn-Co-Ni nanoparticles in N-doped carbon interfacial structures, Chin. J. Catal. 43 (2022) 1316–1323.
[27] S. Zhao, F. Hu, L. Yin, L. Li, S. Peng, Manipulating electron redistribution induced by asymmetric coordination for electrocatalytic water oxidation at a high current density, Sci. Bull. 68 (2023) 1389–1398.
[28] D. Zhang, F. Wang, W. Zhao, M. Cui, X. Fan, R. Liang, Q. Ou, S. Zhang, Boosting hydrogen evolution reaction activity of amorphous molybdenum sulfide under high currents via preferential electron filling induced by tungsten doping, Adv. Sci. 9 (2022) 2202445.
[29] Y. Yan, P. Zhang, Z. Qu, M. Tong, S. Zhao, Z. Li, M. Liu, Z. Lin, Carbon/sulfur aerogel with adequate mesoporous channels as robust polysulfide confinement matrix for highly stable lithium-sulfur battery, Nano Lett. 20 (2020) 7662–7669.
[30] S. Yang, J.-Y. Zhu, X.-N. Chen, M.-J. Huang, S.-H. Cai, J.-Y. Han, J.-S. Li, Self-supported bimetallic phosphides with artificial heterointerfaces for enhanced electrochemical water splitting, Appl. Catal. B Environ. 304 (2022) 120914.
[31] A. Salah, L. Zhang, H. Tan, F. Yu, Z. Lang, N. Al-Ansi, Y. Li, Advanced Ru/Ni/WC@NPC multi-interfacial electrocatalyst for efficient sustainable hydrogen and Chlor-Alkali Co-production, Adv. Energy Mater. 12 (2022) 2200332.
[32] T. Cui, X. Zhai, L. Guo, J.-Q. Chi, Y. Zhang, J. Zhu, X. Sun, L. Wang, Controllable synthesis of a self-assembled ultralow Ru, Ni-doped Fe_2O_3 lily as a bifunctional electrocatalyst for large-current-density alkaline seawater electrolysis, Chin. J. Catal. 43 (2022) 2202–2211.
[33] X. Wang, X. Liu, S. Wu, K. Liu, X. Meng, B. Li, J. Lai, L. Wang, S. Feng, Phosphorus vacancies enriched cobalt phosphide embedded in nitrogen doped carbon matrix enabling seawater splitting at ampere-level current density, Nano Energy 109 (2023) 108292.
[34] H. Sun, Y. Lian, C. Yang, L. Xiong, P. Qi, Q. Mu, X. Zhao, J. Guo, Z. Deng, Y. Peng, A hierarchical nickel-carbon structure templated by metal-organic frameworks for efficient overall water splitting, Energy Environ. Sci. 11 (2018) 2363–2371.
[35] J. Wang, D.T. Tran, K. Chang, S. Prabhakaran, J. Zhao, D.H. Kim, N.H. Kim, J. H. Lee, Hierarchical Ni@CNTs-bridged Mo_xC/Ni_2P heterostructure micro-pillars for enhanced seawater splitting and Mg/seawater battery, Nano Energy 111 (2023) 108440.
[36] J. Chi, L. Guo, J. Mao, T. Cui, J. Zhu, Y. Xia, J. Lai, L. Wang, Modulation of electron structure and dehydrogenation kinetics of nickel phosphide for hydrazine-assisted self-powered hydrogen production in seawater, Adv. Funct. Mater. 33 (2023) 2300625.
[37] J.Y. Zhang, J. Liang, B. Mei, K. Lan, L. Zu, T. Zhao, Y. Ma, Y. Chen, Z. Lv, Y. Yang, C. Yu, Z. Xu, B.Y. Xia, W. Li, Q. Yuan, D. Zhao, Synthesis of Ni/NiO@MoO_{3-x} composite nanoarrays for high current density hydrogen evolution reaction, Adv. Energy Mater. 12 (2022) 2200001.
[38] J. Zhou, M. Wen, R. Huang, Q. Wu, Y. Luo, Y. Tian, G. Wei, Y. Fu, Regulating active hydrogen adsorbed on grain boundary defects of nano-nickel for boosting ammonia electrosynthesis from nitrate, Energy Environ. Sci. 16 (2023) 2611–2620.
[39] Y. Zhang, C. Ma, X. Zhu, K. Qu, P. Shi, L. Song, J. Wang, Q. Lu, A.L. Wang, Hetero-interface manipulation in MoO_x@Ru to evoke industrial hydrogen production performance with current density of 4000 mA cm^{-2}, Adv. Energy Mater. 13 (2023) 2301492.
[40] Y. Liu, X. Liu, A.R. Jadhav, T. Yang, Y. Hwang, H. Wang, L. Wang, Y. Luo, A. Kumar, J. Lee, H.T.D. Bui, M. Gyu Kim, H. Lee, Unraveling the function of metal-amorphous support interactions in single-atom electrocatalytic hydrogen evolution, Angew. Chem. Int. Ed. 61 (2022) e202114160.
[41] F. He, Y. Zhao, X. Yang, S. Zheng, B. Yang, Z. Li, Y. Kuang, Q. Zhang, L. Lei, M. Qiu, L. Dai, Y. Hou, Metal-Organic frameworks with assembled bifunctional microreactor for charge modulation and strain generation toward enhanced oxygen electrocatalysis, ACS Nano 16 (2022) 9523–9534.
[42] X. Kang, F. Yang, Z. Zhang, H. Liu, S. Ge, S. Hu, S. Li, Y. Luo, Q. Yu, Z. Liu, Q. Wang, W. Ren, C. Sun, H.-M. Cheng, B. Liu, A corrosion-resistant RuMoNi catalyst for efficient and long-lasting seawater oxidation and anion exchange membrane electrolyzer, Nat. Commun. 14 (2023) 3607.
[43] Y. Song, M. Sun, S. Zhang, X. Zhang, P. Yi, J. Liu, B. Huang, M. Huang, L. Zhang, Alleviating the work function of vein-Like Co_XP by Cr doping for enhanced seawater electrolysis, Adv. Funct. Mater. 33 (2023) 2214081.
[44] L. Yang, R. He, X. Wang, T. Yang, T. Zhang, Y. Zuo, X. Lu, Z. Liang, J. Li, J. Arbiol, P.R. Martínez-Alanis, X. Qi, A. Cabot, Self-supported NiO/CuO electrodes to boost urea oxidation in direct urea fuel cells, Nano Energy 115 (2023) 108714.
[45] Z. Zhou, Y.-N. Xie, L. Sun, Z. Wang, W. Wang, L. Jiang, X. Tao, L. Li, X.-H. Li, G. Zhao, Strain-induced in situ formation of NiOOH species on Co-Co bond for selective electrooxidation of 5-hydroxymethylfurfural and efficient hydrogen production, Appl. Catal. B Environ. 305 (2022) 121072.